TU Delft

Delft University of Technology

Quantum Transport Properties of Industrial Si 28 / Si O2 28

Sabbagh, D.; Massa, L.; Amitonov, S. V.; Boter, J. M.; Droulers, G.; Eenink, H. G.J.; Veldhorst, M.; Vandersypen, L. M.K.; Scappucci, G.

DOI
10.1103/PhysRevApplied.12.014013

Publication date
2019

Document Version
Final published version

Published in
Physical Review Applied

Citation (APA)
Sabbagh, D., Massa, L., Amitonov, S. V., Boter, J. M., Droulers, G., Eenink, H. G. J., Veldhorst, M., Vandersypen, L. M. K., & Scappucci, G. (2019). Quantum Transport Properties of Industrial Si 28 / Si O2 28. *Physical Review Applied*, *12*(1), Article 014013. https://doi.org/10.1103/PhysRevApplied.12.014013

Important note
To cite this publication, please use the final published version (if applicable).
Please check the document version above.

Copyright
Other than for strictly personal use, it is not permitted to download, forward or distribute the text or part of it, without the consent of the author(s) and/or copyright holder(s), unless the work is under an open content license such as Creative Commons.

Takedown policy
Please contact us and provide details if you believe this document breaches copyrights.
We will remove access to the work immediately and investigate your claim.

This work is downloaded from Delft University of Technology.
For technical reasons the number of authors shown on this cover page is limited to a maximum of 10.

Quantum Transport Properties of Industrial $^{28}Si/^{28}SiO_2$

D. Sabbagh,[1] N. Thomas,[2] J. Torres,[2] R. Pillarisetty,[2] P. Amin,[2] H.C. George,[2] K. Singh,[2] A. Budrevich,[2] M. Robinson,[2] D. Merrill,[2] L. Ross,[2] J. Roberts,[2] L. Lampert,[2] L. Massa,[1] S.V. Amitonov,[1] J.M. Boter,[1] G. Droulers,[1] H.G.J. Eenink,[1] M. van Hezel,[3] D. Donelson,[4] M. Veldhorst,[1] L.M.K. Vandersypen,[1] J.S. Clarke,[2] and G. Scappucci[1,*]

[1] *QuTech and Kavli Institute of Nanoscience, Delft University of Technology, PO Box 5046, 2600 GA Delft, Netherlands*

[2] *Intel Corporation, Technology and Manufacturing Group, Hillsboro, Oregon, 97124, USA*

[3] *URENCO Stable Isotopes, PO Box 158, 7600 AD Almelo, Netherlands*

[4] *Air Liquide Advanced Materials North Branch, Branchburg, New Jersey 08876, USA*

(Received 21 January 2019; revised manuscript received 26 March 2019; published 9 July 2019)

We investigate the structural and quantum transport properties of isotopically enriched $^{28}Si/^{28}SiO_2$ stacks deposited on 300-mm Si wafers in an industrial CMOS fab. Highly uniform films are obtained with an isotopic purity greater than 99.92%. Hall-bar transistors with an oxide stack comprising 10 nm of $^{28}SiO_2$ and 17 nm of Al_2O_3 (equivalent oxide thickness of 17 nm) are fabricated in an academic cleanroom. A critical density for conduction of 1.75×10^{11} cm^{-2} and a peak mobility of 9800 cm^2/Vs are measured at a temperature of 1.7 K. The $^{28}Si/^{28}SiO_2$ interface is characterized by a roughness of $\Delta = 0.4$ nm and a correlation length of $\Lambda = 3.4$ nm. An upper bound for valley splitting energy of 480 μeV is estimated at an effective electric field of 9.5 MV/m. These results support the use of wafer-scale $^{28}Si/^{28}SiO_2$ as a promising material platform to manufacture industrial spin qubits.

DOI: 10.1103/PhysRevApplied.12.014013

I. INTRODUCTION

Enrichment of the spin-zero ^{28}Si isotope drastically reduces spin-bath decoherence in silicon [1,2] and has enabled solid-state spin qubits with extremely long coherence [3,4] and high control fidelity [5–7]. The limited availability of isotopically enriched ^{28}Si in industrially adopted forms [8], however, was previously thought to be a major bottleneck to leverage CMOS technology for manufacturing qubits with the quality and in the large numbers required for fault-tolerant quantum computation [9,10]. Recently, isotopically enriched silane ($^{28}SiH_4$) has been employed in a preindustrial CMOS facility to deposit high-quality ^{28}Si epiwafers [11]. Crucially, an industrial supply of $^{28}SiH_4$ has been established and silicon quantum dots were fabricated on a wafer-scale $^{28}Si/^{28}SiO_2$ stack grown in an industrial manufacturing CMOS fab [12]. In these quantum dots, a single-electron spin lifetime of 2.8 ms was obtained at a temperature of 1.1 K and weak charge noise was measured, pointing to a promising material platform for qubit operation at elevated temperatures.

Studies devoted to ^{28}Si quantum dots, however, tend to discuss only marginally the structural properties of the originating $^{28}Si/^{28}SiO_2$ material stack and the electrical transport in the associated 2DEG. In this paper we provide structural characterization of the same industrial ^{28}Si wafer used for quantum dots in Ref. [12] and assess the disorder properties of the critical $^{28}Si/^{28}SiO_2$ interface. By investigating the quantum transport properties of Hall-bar transistors, we extract key material metrics such as carrier mobility, critical density, interface roughness, interface correlation length, and valley splitting energy. Electron mobility is typically used as a figure of merit to assess the quality of the semiconductor-oxide interface. However, peak mobility is measured at high electron density, where screening effects are relevant [13,14]. The critical density, instead, indicates the minimum density required to establish metallic conduction by overcoming electron trapping at the oxide interface. As such, the critical density is a complementary metric to the mobility and characterizes the interface disorder at low densities, where quantum devices typically operate. Overall, large mobility and small critical density indicate material uniformity and low disorder at the confining interfaces. These properties are beneficial for obtaining reproducible quantum dots at intended locations on the substrate. Valley splitting quantifies the energetic separation between the ground state used for computation and the lowest excited state. A sharp flat interface is required to achieve large splitting energy, which is beneficial for qubit operation [15,16]. The results reported

*g.scappucci@tudelft.nl

 © 2019 American Physical Society

in this work indicate a low disorder environment at the $^{28}Si/^{28}SiO_2$ interface and potential to achieve large valley splitting, supporting the industrial integration of spin qubits on wafer-scale ^{28}Si.

II. MATERIAL CHARACTERIZATION

The schematics in Fig. 1 illustrate the key steps in the supply chain of isotopically enriched precursors for wafer-scale epitaxial growth of ^{28}Si. A silicon-tetrafluoride gas (SiF_4) with natural abundance of ^{28}Si of 92.23% is isotopically enriched in ^{28}Si to a concentration greater than 99.92% by centrifuge separation. The $^{28}SiF_4$, with a residual ^{29}Si concentration of 0.08%, is then reduced to obtain high purity $^{28}SiH_4$. $^{28}SiH_4$ gas cylinders (1% dilution in H_2) have been installed for use in a state-of-the-art chemical-vapor deposition tool of a 300-mm fabrication line to deposit ^{28}Si epilayers. Maintaining the chemical purity of gas precursors throughout the supply chain is crucial to obtain a low disorder $^{28}Si/^{28}SiO_2$ stack. The growth process starts with the deposition of 1 μm of intrinsic natural Si on a high-resistivity 300-mm Si(100) wafer followed by a 100-nm-thick intrinsic ^{28}Si epilayer. The wafer is then thermally processed at high temperature for the formation of a high-quality 10-nm-thick $^{28}SiO_2$ layer. The oxidation process is based on prior Intel transistor technology [17–19]. In this work, the allowed thermal budget for oxidation is optimized [20] to minimize Si self-diffusion and obtain sharp isotopic profiles, as evident in the secondary ion mass spectroscopy profiles in Fig. 1.

In Fig. 1 we compare morphology and composition of the grown stack at the center and the edge of the 300-mm wafer. No difference in surface or interface roughness, composition, and purity can be observed across the wafer, indicating a uniform film deposition. Atomic force microscopy shows a uniform and near defect-free surface with a root-mean-square surface roughness of 0.2 nm measured over an area of 1 μm $\times$ 1 μm. Secondary ion mass spectroscopy of isotopes ^{28}Si, ^{29}Si, and ^{30}Si shows a high-purity film with a residual concentration of nonzero-spin nuclei ^{29}Si reduced from 4.76% in the Si buffer to 0.08% in the purified epilayer, demonstrating that the precursor purity is preserved during the deposition process. The concentration of common background contaminants C and O is below the detection limit of 4×10^{17} cm^{-3} and 1×10^{18} cm^{-3}, respectively. Background doping from P and B is also below the detection limit of 3×10^{15} cm^{-3} and 1×10^{14} cm^{-3}, respectively. High-resolution transmission electron microscopy shows that no dislocations or stacking faults are visible in the epilayer. Moreover, the $^{28}Si/^{28}SiO_2$ interface is flat down to one–two atomic layers over distances ($\simeq$200 nm) that are larger than the

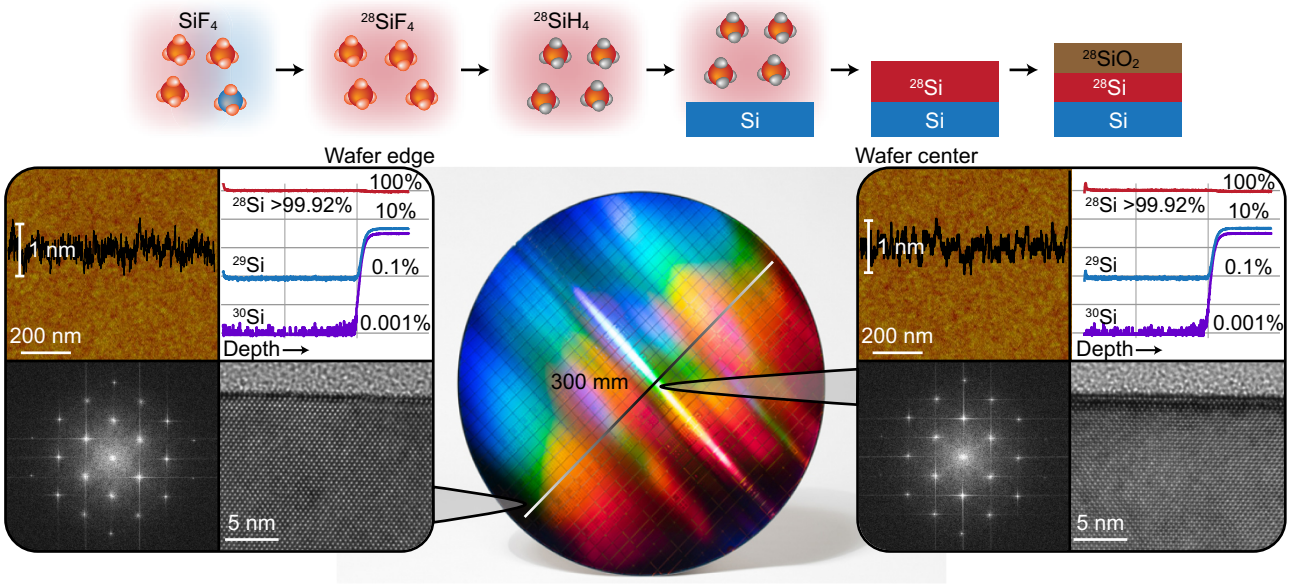

FIG. 1. Central panel: a 300-mm Si(100) wafer with epitaxial ^{28}Si. Top panel: supply chain for $^{28}SiH_4$ gas precursor, starting from a natural SiF_4 with small concentration of ^{29}Si (blue), which is enriched in ^{28}Si (red). The gas is reduced to obtain $^{28}SiH_4$ and then used to deposit the ^{28}Si epilayer followed by thermal oxidation. Atoms of F and H are depicted in orange and gray, respectively. Side panels show the material characterization at the center and at the edge of the as-grown wafer (right and left panels, respectively). The characterization includes (from top left, clockwise): atomic force microscopy of the smooth surface, including a line scan showing the vertical profile with maximum excursion of 1 nm; compositional analysis (depth range of 160 nm) by secondary ion mass spectroscopy of isotopes ^{28}Si (red), ^{29}Si (blue), ^{30}Si (purple); high-resolution transmission electron microscope image of the $^{28}Si/^{28}SiO_2$ interface; electron diffraction patterns with sharp and equally spaced peaks.

typical size of Si quantum-dot spin qubits (≤50 nm). This increases the chance of defining a quantum dot in a step-free area, which is beneficial for obtaining large valley splitting [15,16]. The sharpness of the interface, the negligible density of defects in the lattice, and the associated electron diffraction pattern highlight the film quality and the good control over the growth process despite the introduction of a new Si precursor in the manufacturing CMOS fab.

III. DEVICE FABRICATION AND TRANSPORT PROPERTIES

Moving on to device fabrication, Fig. 2(a) shows schematics and optical micrograph of a MOS transistor shaped in a Hall-bar geometry to investigate the magneto-transport properties of the 2DEG at the $^{28}Si/^{28}SiO_2$ interface. The device was fabricated in an academic clean-room environment, starting from coupon-sized samples diced from the original $^{28}Si/^{28}SiO_2$ 300-mm wafer. We employ e-beam lithography and lift-off additive techniques to resemble the process flow used to fabricate quantum dots as in Ref. [12]. Highly doped n^{++} regions are obtained by P-ion implantation followed by 30 s of activation anneal at 1000 °C in N_2 environment. Multiple ohmic contacts are deposited on the implant regions by e-beam evaporation of Al. An additional Al_2O_3 layer of 17 nm is deposited by atomic layer deposition at 300 °C, so that the $^{28}Si/^{28}SiO_2$ interface undergoes similar processing as in the fabrication of multilayer gate-defined qubits [12]. The resulting dielectric stack has an equivalent oxide thickness of 17 nm. A Ti/Pd top gate is deposited to define a Hall-bar geometry with a 100-μm-wide and 500-μm-long central region. The last processing step is a forming gas anneal at 400 °C to reduce the damage induced by e-beam lithography [14,21].

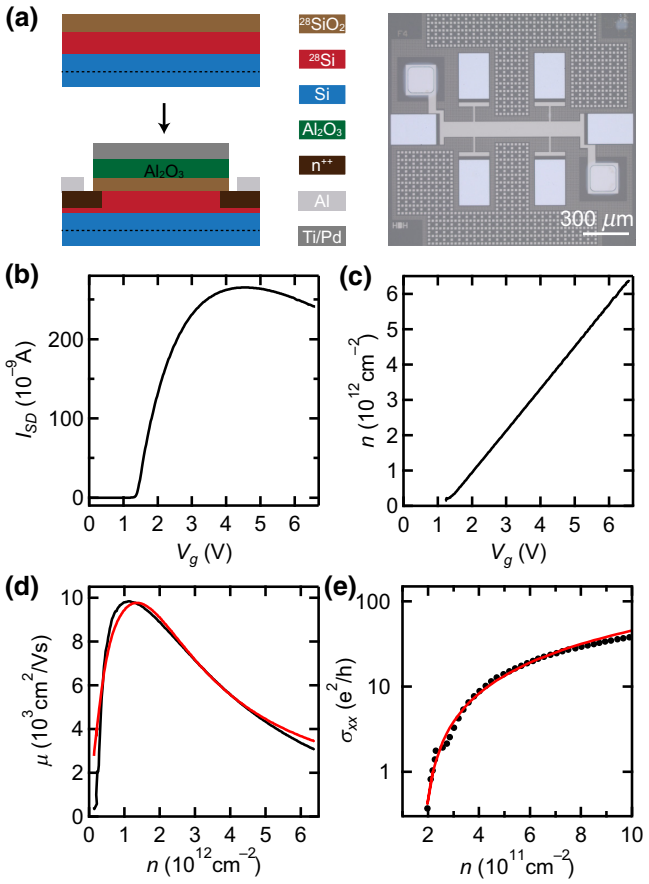

FIG. 2. (a) Schematics of the Hall-bar device fabrication, starting from the 300-mm $^{28}SiO_2/^{28}Si/Si(100)$ stack followed by coupon-sized processing. The optical micrograph of the final device shows the multiterminal geometry used for Hall measurements. (b) Source-drain current I_{SD} measured as a function of top gate voltage V_g at $T = 1.7$ K. (c) Linear relationship between 2DEG Hall density n and top gate voltage V_g. (d) Channel mobility μ measured as a function of n (black) and corresponding calculation (red) including scattering from charged impurities and from interface roughness. (e) 2DEG conductivity in the low density range (black) and fit to percolation theory (red).

The electrical characterization of the device is performed at a temperature of 1.7 K using standard four-terminal low-frequency lock-in techniques with a constant source-drain excitation voltage of 1 mV. Longitudinal (ρ_{xx}) and transverse (R_{xy}) resistivity are measured as a function of carrier density—controlled by the top gate—and external perpendicular magnetic field B. The Hall carrier density n and the electron mobility μ are calculated using the relationships $R_{xy} = (ne)^{-1}B$ and $\mu = (ne\rho_0)^{-1}$, respectively, where e is the elementary charge and $\rho_0 = \rho_{xx}(B = 0\ \mathrm{T})$.

A dc voltage applied to the top gate (V_g) accumulates a 2DEG at the $^{28}Si/^{28}SiO_2$ interface, which conducts above a turn-on voltage of $V_{TO} = 1.22$ V [22], as shown in Fig. 2(b). For values below V_{TO} no current flow is observed in the device up to a temperature of $T = 23$ K, confirming the insulating behavior of the intrinsic ^{28}Si film at low temperature. For $V_g > V_{TO}$ [Fig. 2(c)] we measure a linear increase in the Hall density n as a function of V_g. The experimental capacitance $C = e\ dn/dV_g = 0.19\ \mu\mathrm{F/cm^2}$ matches within 5% of the expected value for the given dielectric stack. Upon multiple sweeps of V_g no hysteresis is observed and the same values of V_{TO} and C are measured, indicating a stable potential landscape at the oxide interface.

The experimental and theoretically calculated density-dependent mobility curves are shown in Fig. 2(d). Above a critical density, required to establish metallic conduction in the 2DEG, the mobility rises sharply due to screening from charged impurity Coulomb scattering [23–26]. A peak mobility of 9800 cm^2/Vs is reached at $n = 1.13 \times 10^{12}$ cm^{-2}, corresponding to a mean free path of 120 nm. Beyond, the mobility drops due to surface-roughness scattering at the $^{28}Si/^{28}SiO_2$ interface [23,25,26]. The calculated scattering-limited mobility takes into account a scattering charge density at the semiconductor-oxide

TABLE I. Comparison of material stack, device characteristics, and low-temperature electrical transport properties in Si MOS Hall-bar transistors obtained by different groups. Material stack description includes thicknesses t of the first dielectric (SiO_2) and eventually of the second dielectric (Al_2O_3). We also indicate whether or not quantum dots have been fabricated on the same wafer.

Reference	Channel material	t_{SiO_2} (nm)	$t_{Al_2O_3}$ (nm)	E-beam & forming gas	Mobility (cm^2/Vs)	T (K)	Critical density (10^{11} cm^{-2})	Quantum-dot fabrication
This work	99.92% ^{28}Si-epi	10	17	Yes	9800	1.7	1.75	Yes [12]
Ref. [27]	99.95% ^{28}Si-epi	35	0	No	11 600	N/A	1.60	Yes
Ref. [28]	^{28}Si-epi	110	0	N/A	14 000	4.2	N/A	No
Ref. [21]	Si bulk	35	60	Yes	8300	4.2	N/A	Yes
Ref. [14]	Si bulk	30	0	Yes	14 000	0.335	0.95[a]	Yes [29]
Ref. [14]	Si bulk	30	0	No	23 000	0.335	0.83[a]	Yes [29]
Ref. [13]	Si bulk	35	0	No	15 000	0.25	1.04[a]	No
Ref. [13]	Si bulk	10	0	No	10 000	0.25	N/A	No
Ref. [30]	Si bulk	190	0	N/A	34 000	0.3	N/A	No
Ref. [31]	Si bulk	50	0	N/A	19 500	4	N/A	Yes

[a]Percolation transition density extrapolated at $T = 0$.

interface and an exponential autocorrelation function form of the interface roughness [13,25,26]. A good match is obtained for a scattering charge density of 4.65×10^{10} cm^{-2}, an interface roughness of $\Delta = 0.4$ nm, and an interface correlation length of $\Lambda = 3.4$ nm (see Appendix). Δ describes the interface root-mean-square height fluctuations, Λ is the lateral distance over which the fluctuations are correlated. The interface roughness is compatible with the morphology investigation by transmission electron microscopy reported in Fig. 1.

The critical density is extracted from a percolation fit of the density-dependent conductivity [Fig. 2(e)] $\sigma_{xx} \sim (n - n_p)^p$ [13,14], where n_p, p are the percolation transition density and exponent, respectively. By fixing $p = 1.31$, as expected in a two-dimensional system, we estimate $n_p = 1.75 \pm 0.02 \times 10^{11}$ cm^{-2} at $T = 1.7$ K. The fit used to estimate n_p is performed over the density range 2.0–7.3 $\times$ 10^{11} cm^{-2} (see Appendix). Previous studies have shown that n_p decreases with decreasing temperature [13,14], therefore the obtained value of 1.75×10^{11} cm^{-2} sets an upper bound for the critical density in the temperature regime at which qubits are typically operated ($T \leq$ 100 mK).

Both the mobility and critical density obtained in the wafer-scale isotopically enriched $^{28}Si/^{28}SiO_2$ stack are qualitatively comparable to the values previously reported for high-mobility Si MOSFETs at low temperatures [13,14,21,27,28,30,31] (see Table I). In drawing a meaningful comparison with the data reported in the literature, the reader should consider material stacks that have produced quantum-dot devices using a similar process flow. For example, peak mobility is known to be higher in devices with thicker oxide [23,32] and degrades upon device exposure to e-beam [14,21].

Transport characterization at high magnetic field (Fig. 3) allows the measurement of effective mass m^* and quantum lifetime τ_q, from which we estimate an upper bound for the valley splitting energy and the g factor. In Fig. 3(a) we report the longitudinal magnetoresistivity at a density $n = 1.05 \times 10^{12}$ cm^{-2}, which corresponds to an effective electric field of 9.5 MV/m. Shubnikov-de Haas (SdH) oscillations are observed, with minima aligned to quantum Hall plateaus in R_{xy}. SdH oscillations start at $B_{\text{eff}} = 1$ T and spin degeneracy is resolved at $B_S = 4.3$ T, corresponding to the even filling factor $\nu = 10$. Figure 3(b) shows the filling factor progression against $1/B$. High mobility and density allow filling factors to be resolved up to $\nu = 36$, with fourfold periodicity at low magnetic field due to spin and valley degeneracy and twofold periodicity beyond B_S. We do not observe odd filling factors, indicating that the twofold valley degeneracy is not resolved under these measurement conditions. From the linear filling factor progression we extract a density $n_{\text{SdH}} = 1.06 \times 10^{12}$ cm^{-2}. The agreement between the Hall density n and n_{SdH} indicates that only one high-mobility subband contributes to electrical transport, confirming the high-quality ^{28}Si epitaxy.

The transverse effective mass m^* of the high-mobility carriers is calculated from the damping of the SdH oscillations with increasing temperature, described by the relation [33–36]

$$\frac{\Delta\rho_{xx}(T,B)}{\Delta\rho_{xx}(T_0,B)} = \frac{T\sinh\chi_0}{T_0\sinh\chi}, \tag{1}$$

where $\Delta\rho_{xx}$ is the SdH oscillation amplitude after polynomial background subtraction, $\chi = 2\pi^2 k_B T/\hbar\omega_c$, $\chi_0 = \chi(T_0{=}1.7\text{ K})$, $\omega_c = eB/m^*$ is the cyclotron frequency, $\hbar$ is the Planck constant, and k_B the Boltzmann constant. Figure 3(d) shows the temperature dependence of the oscillation amplitude at $B = 3.18$ T, before spin splitting, normalized to the amplitude at $T_0 = 1.7$ K. By fitting the data to Eq. (1) we obtain an effective mass of $m^* = 0.19m_e$,

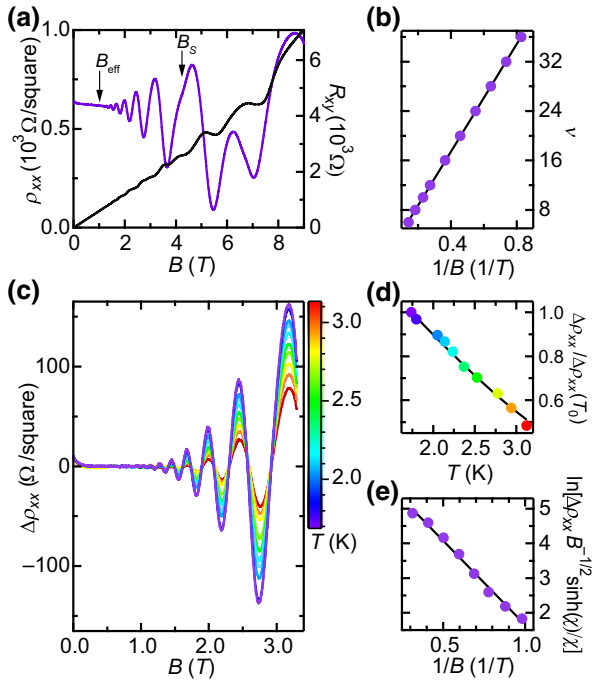

FIG. 3. (a) Longitudinal (ρ_{xx}, purple) and transverse (R_{xy}, black) resistivity at $n = 1.05 \times 10^{12}$ cm^{-2} and $T = 1.7$ K. Arrows indicate the magnetic field at which SdH oscillations and Zeeman spin splitting are resolved. (b) Linear relationship between the filling factors ν and the inverse of magnetic field B. The solid line is the linear fit from which n_{SdH} is calculated. (c) Temperature dependence of the SdH oscillations amplitude in the range $T = 1.7$–3.1 K, after polynomial background subtraction. (d) $\Delta\rho_{xx}$ at $B = 3.18$ T as a function of T, normalized at the value $T = 1.7$ K. The solid line is the fit used to extract m^*. (e) Dingle plot at $T = 1.7$ K, considering the eight most-resolved oscillation maxima. The solid line is the linear fit used to extract τ_q.

where m_e is the free-electron mass, and a transport lifetime $\tau_t = \mu m^*/e = 1.06$ ps. The m^* value is in agreement with measurements performed on natural Si [37] and corresponds to the expected value obtained from band-structure calculations neglecting many-body effects [23].

Once the effective mass is measured, the quantum lifetime τ_q can be determined from the SdH oscillation envelope at T_0, using the relation [33,36]

$$\Delta\rho_{xx}(T_0, B) \sim \sqrt{B}\frac{\chi_0}{\sinh\chi_0}\exp\left(-\frac{\pi}{\omega_c\tau_q}\right). \qquad (2)$$

The Dingle plot of Fig. 3(e) reports the fit from which we extract $\tau_q = 0.69$ ps. This value implies a small Dingle ratio of $\tau_t/\tau_q = 1.54$, indicating that large-angle scattering events are dominant since most sources of scattering are located near the semiconductor-oxide interface. This result confirms the validity of the model used for the theoretically calculated mobility curve of Fig. 2(d) and suggests that scattering associated with the Al_2O_3 deposition is minimal, which is beneficial for quantum-dot fabrication.

From the obtained τ_q we calculate a Landau-level broadening of $\Gamma \approx \hbar/2\tau_q = 480$ μeV, which sets an upper bound to valley splitting at the investigated density (electric field) and magnetic field. For comparison, a valley splitting energy of 275 μeV is measured in ^{28}Si quantum dots fabricated on the same wafer in an academic environment [12] and a valley splitting of 200 μeV is reported for electric fields of 10 MV/m in other quantum dots [38]. The electron g factor is evaluated by considering that the onset of spin splitting at B_S implies a Zeeman energy $g\mu_B B_S \simeq \Gamma$, where μ_B is the Bohr magneton. From this, a g factor of $g = 1.92 \pm 0.07$ is estimated, which is close to the expected single-particle value of $g = 2$.

IV. CONCLUSION

In conclusion, we investigate the structural and quantum transport properties of isotopically enriched ^{28}Si/^{28}SiO$_2$ stacks deposited on 300-mm wafers in an industrial CMOS fab. The material characterization shows that the level of control achieved in the growth process results in a uniform deposition with high-purity epilayers and a sharp semiconductor-oxide interface. Detailed quantum transport characterization of Hall-bar devices fabricated in an academic cleanroom points to a high-quality ^{28}Si/^{28}SiO$_2$ interface, promising for hosting spin qubits. Mobility and critical density for these stacks are among the best reported for gate stacks used for quantum-dot fabrication, with the potential to achieve large valley splitting. Disorder at the critical semiconductor-oxide interface is expected to further decrease by processing the entire gate stack in the high-volume manufacturing environment, because an advanced process control is attainable and e-beam-induced damage is avoided.

ACKNOWLEDGMENTS

M.V. acknowledges support from the Netherlands Organisation of Scientific Research (NWO) Vidi program. L.M.K.V., M.V., and G.S. acknowledge financial support by Intel Corporation.

APPENDIX: THEORETICAL CALCULATIONS AND FITTING PROCEDURES

1. Mobility-density curve

To assess how sensitive the calculated mobility curve is to the input parameters (i.e., interface roughness Δ, interface correlation length Λ, and scattering charge density n_i), in Fig. 4 we show the mobility curve calculated by varying the parameters one at a time, starting from the best values that generated the theoretical curve reported in Fig. 2(d).

The theoretical curve is more sensitive to variations in Δ and n_i, compared to Λ. In fact, a variation of 5% in Δ

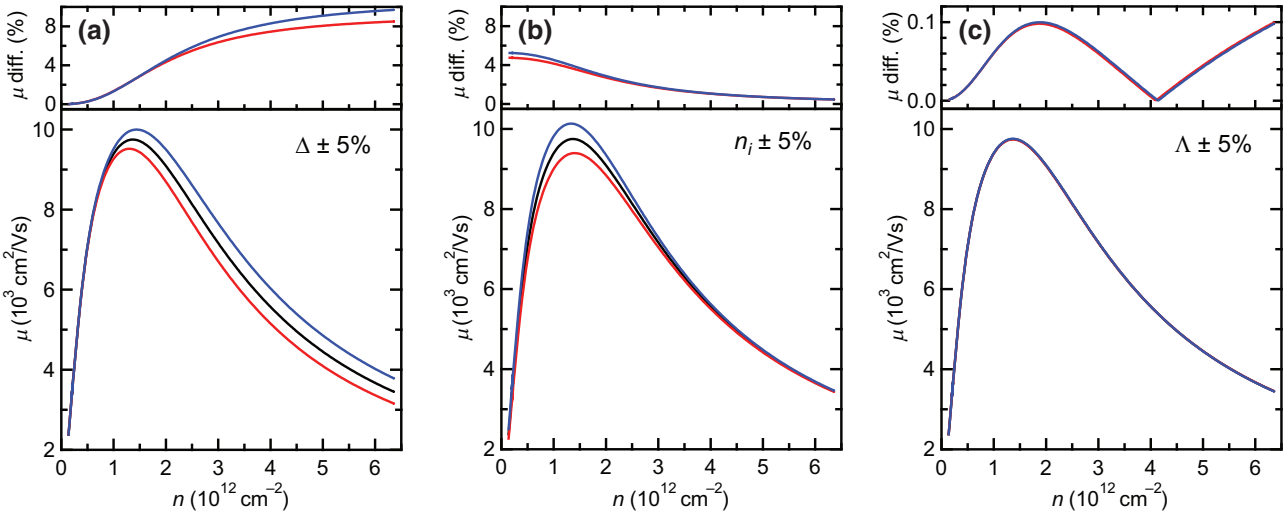

FIG. 4. Bottom panels: density-dependent mobility μ calculated by individually increasing (red curves) and decreasing (blue curves) the parameters Δ (a), n_i (b), and Λ (c) by 5% with respect to the values that generated the theoretical mobility curve in Fig. 2(d), here displayed in black. Upper panels: relative difference between the mobility curve in Fig. 2(d) and the curves obtained by increasing (red curve) and decreasing (blue curve) the parameters by 5%.

or n_i results in a maximum variation in the mobility up to approximately 10% and approximately 5%, respectively. A variation of 5% in Λ results, instead, in a negligible variation in the mobility (0.1%). We note that variations of Λ up to 15% are necessary to induce a mobility variation of only 4%.

2. Percolation transition density

The percolation theory considered to evaluate the percolation transition density n_p is valid only in a density range Δn close to n_p and for $n > n_p$. For this reason, the fit reported in Fig. 2(e) of the main text is performed considering a density range of 2.0–7.3 $\times$ 10^{11} cm^{-2}, resulting in $n_p = 1.75 \pm 0.02 \times 10^{11}$ cm^{-2}.

To clarify how the density range is chosen to fit the data, in Fig. 5 we show n_p as a function of the range over which the fit is performed. The density range Δn is increased by fixing the lowest density at 2.0×10^{11} cm^{-2} and increasing the highest density value. While the error intervals increase for smaller density ranges, the extracted value of n_p shows a weak dependency on the density range used for the fit, with all the values between 1.70×10^{11} cm^{-2} and 1.75×10^{11} cm^{-2}. The chosen value of $n_p = 1.75 \times 10^{11}$ cm^{-2} is therefore a valid estimate since it is extracted considering a significant density range and further extending this range does not result in improvements in the error intervals.

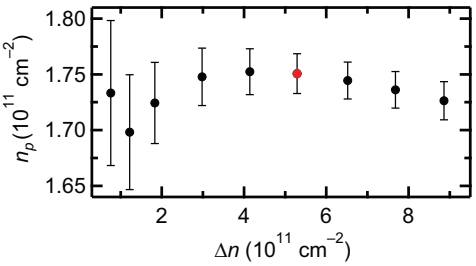

FIG. 5. Extracted percolation density n_p as a function of density range Δn over which the fit is performed. The lower bound of all the density ranges is $n = 2.0 \times 10^{11}$ cm^{-2}. The widest range considered here includes a maximum density of $n = 1.08 \times 10^{12}$ cm^{-2}, close to the value at peak mobility of $n = 1.13 \times 10^{12}$ cm^{-2}. The point in red corresponds to a fit result of $n_p = 1.75 \pm 0.02 \times 10^{11}$ cm^{-2}.

[1] W. M. Witzel, M. S. Carroll, A. Morello, Ł. Cywiński, and S. Das Sarma, Electron Spin Decoherence in Isotope-enriched Silicon, Phys. Rev. Lett. **105**, 187602 (2010).

[2] W. M. Witzel and S. Das Sarma, Quantum theory for electron spin decoherence induced by nuclear spin dynamics in semiconductor quantum computer architectures: Spectral diffusion of localized electron spins in the nuclear solid-state environment, Phys. Rev. B **74**, 035322 (2006).

[3] J. T. Muhonen, J. P. Dehollain, A. Laucht, F. E. Hudson, R. Kalra, T. Sekiguchi, K. M. Itoh, D. N. Jamieson, J. C. McCallum, A. S. Dzurak, and A. Morello, Storing quantum information for 30 seconds in a nanoelectronic device, Nat. Nanotechnol. **9**, 986 (2014).

[4] M. Veldhorst, C. H. Yang, J. C. C. Hwang, W. Huang, J. P. Dehollain, J. T. Muhonen, S. Simmons, A. Laucht, F. E. Hudson, K. M. Itoh, A. Morello, and A. S. Dzurak, A two-qubit logic gate in silicon, Nature **526**, 410 (2015).

[5] M. Veldhorst, J. C. C. Hwang, C. H. Yang, A. W. Leenstra, B. de Ronde, J. P. Dehollain, J. T. Muhonen, F. E. Hudson, K. M. Itoh, A. Morello, and A. S. Dzurak, An addressable quantum dot qubit with fault-tolerant control-fidelity, Nat. Nanotechnol. **9**, 981 (2014).

[6] J. Yoneda, K. Takeda, T. Otsuka, T. Nakajima, M. R. Delbecq, G. Allison, T. Honda, T. Kodera, S. Oda, Y. Hoshi, N. Usami, K. M. Itoh, and S. Tarucha, A quantum-dot spin qubit with coherence limited by charge noise and fidelity higher than 99.9%, Nat. Nanotechnol. **13**, 102 (2018).

[7] W. Huang, C. H. Yang, K. W. Chan, T. Tanttu, B. Hensen, R. C. C. Leon, M. A. Fogarty, J. C. C. Hwang, F. E. Hudson, K. M. Itoh, A. Morello, A. Laucht, and A. S. Dzurak, Fidelity benchmarks for two-qubit gates in silicon, Nature **569**, 532 (2019).

[8] K. M. Itoh and H. Watanabe, Isotope engineering of silicon and diamond for quantum computing and sensing applications, MRS Commun. **4**, 143 (2014).

[9] L. M. K. Vandersypen, H. Bluhm, J. S. Clarke, A. S. Dzurak, R. Ishihara, A. Morello, D. J. Reilly, L. R. Schreiber, and M. Veldhorst, Interfacing spin qubits in quantum dots and donors—hot, dense, and coherent, npj Quantum Inf. **3**, 34 (2017).

[10] R. Li, L. Petit, D. P. Franke, J. P. Dehollain, J. Helsen, M. Steudtner, N. K. Thomas, Z. R. Yoscovits, K. J. Singh, S. Wehner, L. M. K. Vandersypen, J. S. Clarke, and M. Veldhorst, A crossbar network for silicon quantum dot qubits, Sci. Adv. **4**, eaar3960 (2018).

[11] V. Mazzocchi, P. G. Sennikov, A. D. Bulanov, M. F. Churbanov, B. Bertrand, L. Hutin, J. P. Barnes, M. N. Drozdov, J. M. Hartmann, and M. Sanquer, 99.992% ^{28}Si CVD-grown epilayer on 300 mm substrates for large scale integration of silicon spin qubits, J. Cryst. Growth **509**, 1 (2019).

[12] L. Petit, J. M. Boter, H. G. J. Eenink, G. Droulers, M. L. V. Tagliaferri, R. Li, D. P. Franke, K. J. Singh, J. S. Clarke, R. N. Schouten, V. V. Dobrovitski, L. M. K. Vandersypen, and M. Veldhorst, Spin Lifetime and Charge Noise in hot Silicon Quantum dot Qubits, Phys. Rev. Lett. **121**, 076801 (2018).

[13] L. A. Tracy, E. H. Hwang, K. Eng, G. A. Ten Eyck, E. P. Nordberg, K. Childs, M. S. Carroll, M. P. Lilly, and S. Das Sarma, Observation of percolation-induced two-dimensional metal-insulator transition in a Si MOSFET, Phys. Rev. B **79**, 235307 (2009).

[14] J.-S. Kim, A. M. Tyryshkin, and S. A. Lyon, Annealing shallow Si/SiO_2 interface traps in electron-beam irradiated high-mobility metal-oxide-silicon transistors, Appl. Phys. Lett. **110**, 123505 (2017).

[15] D. Culcer, X. Hu, and S. Das Sarma, Interface roughness, valley-orbit coupling, and valley manipulation in quantum dots, Phys. Rev. B **82**, 205315 (2010).

[16] C. H. Yang, A. Rossi, R. Ruskov, N. S. Lai, F. A. Mohiyaddin, S. Lee, C. Tahan, G. Klimeck, A. Morello, and A. S. Dzurak, Spin-valley lifetimes in a silicon quantum dot with tunable valley splitting, Nat. Commun. **4**, 2069 (2013).

[17] M. Bohr, S. Ahmed, L. Brigham, R. Chau, R. Gasser, R. Green, W. Hargrove, E. Lee, R. Natter, S. Thompson, and K. Weldon, in *Proceedings of 1994 IEEE International Electron Devices Meeting* (IEEE, 1994), p. 273.

[18] M. Bohr, S. S. Ahmed, S. U. Ahmed, M. Bost, T. Ghani, J. Greason, R. Hainsey, C. Jan, P. Packan, S. Sivakumar, and S. Thompson, in *International Electron Devices Meeting. Technical Digest* (IEEE, 1996), p. 847.

[19] S. Yang, S. Ahmed, B. Arcot, R. Arghavani, P. Bai, S. Chambers, P. Charvat, R. Cotner, R. Gasser, T. Ghani, and M. Hussein, in *International Electron Devices Meeting 1998. Technical Digest (Cat. No. 98CH36217)* (IEEE, 1998), p. 197.

[20] Further details of the oxidation process are considered a trade secret and are not reported in this paper.

[21] E. P. Nordberg, G. A. Ten Eyck, H. L. Stalford, R. P. Muller, R. W. Young, K. Eng, L. A. Tracy, K. D. Childs, J. R. Wendt, R. K. Grubbs, J. Stevens, M. P. Lilly, M. A. Eriksson, and M. S. Carroll, Enhancement-mode double-top-gated metal-oxide-semiconductor nanostructures with tunable lateral geometry, Phys. Rev. B **80**, 115331 (2009).

[22] The observed turn-on voltage of 1.22 V matches with the value of 1.15 V obtained by TCAD simulations considering the actual gate stack at cryogenic temperature and an intrinsic epitaxial layer. These results suggest there is no significant built-in charge-dependent threshold shift. Further agreement with experiments ($V_{TO} = 1.20$ V) is obtained taking into account a background doping density of 1×10^{14} cm^{-3}.

[23] T. Ando, A. B. Fowler, and F. Stern, Electronic properties of two-dimensional systems, Rev. Mod. Phys. **54**, 437 (1982).

[24] A. Gold, Peak Mobility of Silicon Metal-oxide-semiconductor Systems, Phys. Rev. Lett. **54**, 1079 (1985).

[25] A. Gold and V. T. Dolgopolov, Temperature dependence of the conductivity for the two-dimensional electron gas: Analytical results for low temperatures, Phys. Rev. B **33**, 1076 (1986).

[26] G. H. Kruithof, T. M. Klapwijk, and S. Bakker, Temperature and interface-roughness dependence of the electron mobility in high-mobility Si (100) inversion layers below 4.2 K, Phys. Rev. B **43**, 6642 (1991).

[27] S. Rochette, M. Rudolph, A.-M. Roy, M. J. Curry, G. A. Ten Eyck, R. P. Manginell, J. R. Wendt, T. Pluym, S. M. Carr, D. R. Ward, M. P. Lilly, M. S. Carroll, and M. Pioro-Ladrière, Quantum dots with split enhancement gate tunnel barrier control, Appl. Phys. Lett. **114**, 083101 (2019).

[28] S. Shankar, A. M. Tyryshkin, J. He, and S. A. Lyon, Spin relaxation and coherence times for electrons at the Si/SiO_2 interface, Phys. Rev. B **82**, 195323 (2010).

[29] J.-S. Kim, T. M. Hazard, A. A. Houck, and S. A. Lyon, A low-disorder metal-oxide-silicon double quantum dot, Appl. Phys. Lett. **114**, 043501 (2019).

[30] V. M. Pudalov, M. E. Gershenson, H. Kojima, N. Butch, E. M. Dizhur, G. Brunthaler, A. Prinz, and G. Bauer, Low-density Spin Susceptibility and Effective Mass of Mobile Electrons in Si Inversion Layers, Phys. Rev. Lett. **88**, 196404 (2002).

[31] M. J. Curry, M. Rudolph, T. D. England, A. M. Mounce, R. M. Jock, C. Bureau-Oxton, P. Harvey-Collard, P. A. Sharma, J. M. Anderson, D. M. Campbell, J. R. Wendt, D. R. Ward, S. M. Carr, M. P. Lilly, and M. S. Carroll, Single-shot readout performance of two heterojunction-bipolar-transistor amplification circuits at millikelvin temperatures, arXiv:1901.04570 (2019).

[32] A. Yagi and S. Kawaji, Oxide thickness effects on electron scatterings at a thermally grown $Si-SiO_2$ interface, Appl. Phys. Lett. **33**, 349 (1978).

[33] G. Bauer and H. Kahlert, Low-temperature non-ohmic galvanomagnetic effects in degenerate n-type InAs, Phys. Rev. B **5**, 566 (1972).

[34] A. Isihara and L. Smrcka, Density and magnetic field dependences of the conductivity of two-dimensional electron systems, J. Phys. C: Solid State Phys. **19**, 6777 (1986).

[35] P. T. Coleridge, Small-angle scattering in two-dimensional electron gases, Phys. Rev. B **44**, 3793 (1991).

[36] O. Celik, E. Tiras, S. Ardali, S. B. Lisesivdin, and E. Ozbay, Determination of the in-plane effective mass and quantum lifetime of 2D electrons in AlGaN/GaN based HEMTs, Phys. Status Solidi C **8**, 1625 (2011).

[37] F. F. Fang, A. B. Fowler, and A. Hartstein, Effective mass and collision time of (100) Si surface electrons, Phys. Rev. B **16**, 4446 (1977).

[38] J. K. Gamble, P. Harvey-Collard, N. T. Jacobson, A. D. Baczewski, E. Nielsen, L. Maurer, I. Montaño, M. Rudolph, M. S. Carroll, C. H. Yang, A. Rossi, A. S. Dzurak, and R. P. Muller, Valley splitting of single-electron Si MOS quantum dots, Appl. Phys. Lett. **109**, 253101 (2016).